



NiO-based sensor for in situ CO monitoring above 1000 °C: behavior and mechanism

Yi Wang¹ · Liang Ma^{1,2} · Wei Li¹ · Angela M. Deibel¹ · Wenyuan Li³ · Hanchen Tian¹ · Xingbo Liu¹

Received: 12 March 2022 / Revised: 22 April 2022 / Accepted: 26 April 2022 / Published online: 5 May 2022
© The Author(s), under exclusive licence to Springer Nature Switzerland AG 2022

Abstract

An advanced smart sensor network is essential to a combustion system, which favors in situ, locally placed, and low-cost gas sensors. However, most chemical/electrochemical sensors fail to work in a combustion boiler, due to demanding operation temperatures (> 1000 °C). This work, for the first time, reports a well-functioning mixed-potential type CO sensor at 1000–1200 °C using nickel oxide (NiO) as the sensing material on the yttrium-stabilized zirconium (YSZ) oxide electrolyte. The influences of feed flow rate, electrode thickness, and porosity on the sensor behavior were investigated and the developed mixed potential gas sensor delivered notable and fast responses to 1000 ppm CO in 3% O₂: 109 mV @ 1000 °C, 40 mV @ 1100 °C, and 7 mV @ 1200 °C. The sensing mechanism was identified different from the common theory based on CO oxidation coupled with oxygen reduction. A new mechanism is attributed to the inverse reactions: CO reduction coupled with oxygen evolution. For the first time, an inversion temperature was found for the CO-NiO reaction. Below the inversion temperature, CO oxidation occurs as commonly presented. Above the inversion temperature, CO is electrochemically reduced over NiO into carbon and oxygen ions, evidenced by electrochemical and compositional characterizations. The results can complement CO sensing mechanisms for mixed potential sensors and further trigger more research efforts to expand the working temperature limit of mixed potential sensors for practical application in combustion control systems.

Keywords Carbon monoxide sensor · Mixed-potential gas sensor · Nickel oxide · Combustion process

1 Introduction

Among the global endeavors to achieve carbon neutrality, fossil fuel (coal, oil, and natural gas)-based combustion processes still play a significant role in energy supply for the foreseeable future [1]. Sectors responsible for the largest carbon and pollutant emissions, such as electricity,

industry, and transportation [2, 3], should optimize their fossil fuel utilization efficiency and reduce their environmental footprints and accompanied pollution [4–10]. An advanced combustion monitor and control system can contribute to an improved combustion process and overall efficiency. With the installation of a digital optimization network, heat and boiler efficiency increased by 1.08% and 0.93%, respectively, for the JK Spruce Station Unit Number 1 (566 MW) at Calaveras Power [11]. This installation is capable of reducing 12 kilotons of CO₂ emissions a year (assuming a 5000-h full-load operation).

Diverse sensors based on multifunctional metal oxides, polymers, and composites have been widely applied in many fields [12–24]. Gas sensors are core components for combustion feedback control networks since some specific gases are the direct indicators of a firing process. For example, the gas compositions of an optimum operating condition of a coal-fired power plant boiler are around 1–2% O₂ and 100–200 ppm CO depending on coal types [25]. Therefore, a superior gas sensor network to ensure a high-efficiency combustion process would require the

Yi Wang, Liang Ma and Wei Li contributed equally to this work.

✉ Xingbo Liu
xingbo.liu@mail.wvu.edu

¹ Department of Mechanical and Aerospace Engineering, Benjamin M. Statler College of Engineering and Mineral Resources, West Virginia University, Morgantown, West Virginia 26506, USA

² School of Materials Science and Engineering, Hebei University of Engineering, Handan 056038, China

³ Department of Chemical and Biomedical Engineering, Benjamin M. Statler College of Engineering and Mineral Resources, West Virginia University, Morgantown, West Virginia 26506, USA

utilization of multiple robust, in situ gas sensors (operation temperature $> 1000\text{ }^{\circ}\text{C}$) [26]. In this case, burners in the boiler could be individually controlled to adjust the fuel/air ratio, targeting the locally deviated firing process, based on the real-time feedback of on-site sensors [26]. Current commonly implemented sensor and control systems utilize extraction techniques to analyze the composition of flue gases, which presents average feedback with an obvious delay [27, 28]. Chemical resistive sensors, which are widely utilized at lower temperatures ($< 500\text{ }^{\circ}\text{C}$) [12, 13, 29–37], cannot maintain chemical stability in combustion boilers. Optical sensing methods, e.g., tunable diode or quantum cascade laser spectroscopies, can give fast responses to varied gases. However, the challenges are that the large amounts of substances impede light transmission and the measured value is not local, but an average value among the light path [38]. Mixed potential sensors based on oxygen ion-conducting yttrium-stabilized zirconium oxide (YSZ) are suitable for high temperatures [26]. However, those YSZ-based mixed potential sensors do not show good performances in temperatures higher than $900\text{ }^{\circ}\text{C}$, because the chemical durability and sensitivity of sensing materials cannot sustain [39–49].

Since CO concentration, in addition to O_2 content, is a direct indicator of a combustion process, an in situ high-temperature CO sensor is of interest. Our previous work reported the use of NiO as the sensing electrode, achieving a 36 mV sensing response to 1000 ppm CO at $1000\text{ }^{\circ}\text{C}$, and for the first time proposed a CO reduction-based sensing mechanism [26]. However, the mechanism needed more thorough investigation since CO reduction is not thermodynamically favorable, and the performance can be improved upon further.

In the present work, multiple electrochemical and microscopic measurements are used to unveil the particular CO sensing mechanism on NiO. CO electrochemically reduces over NiO into carbon and oxygen ions with the produced carbon dissolving into the NiO lattice at $1000\text{--}1200\text{ }^{\circ}\text{C}$. CO reduction couples with an oxygen evolution reaction to form the mixed potential (sensing signal). An intriguing inversion temperature is found for the CO-NiO reaction for the first time, which integrates the commonly reported CO oxidation mechanism and the proposed CO reduction mechanism. In the end, NiO as the sensing electrode is notably optimized via a more comprehensive investigation on the factors affecting sensitivity, such as feed flow rate, electrode thickness, porosity, and oxygen content. Marked and fast responses of the mixed potential sensor to 1000 ppm CO in 3% O_2 of improved NiO are achieved: 109 mV @ $1000\text{ }^{\circ}\text{C}$, 40 mV @ $1100\text{ }^{\circ}\text{C}$, and 7 mV @ $1200\text{ }^{\circ}\text{C}$.

2 Experimental section

2.1 Sensor fabrication

The mixed potential-type sensor structure is shown in Fig. 1a, which consists of an 8YSZ electrolyte, a porous NiO electrode on the sensing side, and a porous Pt electrode on the reference side. A dense circle YSZ pellet with a diameter of 13 mm and thickness of 2 mm was fabricated at first by mechanical pressing of YSZ powder (Tosoh, yttria-stabilized zirconia, TZ-8YSB, 8 mol% Y_2O_3 in zirconia) followed by $1400\text{ }^{\circ}\text{C}$ sintering in air for 2 h. Then, each circular electrode was made one by one by screen-printing the electrode material slurries onto the electrolyte followed by 2 h $1400\text{ }^{\circ}\text{C}$ annealing in air. The Pt electrode on the reference side was 6.5 mm in diameter, while the NiO electrode was 6 mm in diameter. NiO slurry was made by mixing the commercial NiO powders (fuel cell materials, NiO-F fine grade, 99%, particle size $0.5\text{--}1.5\text{ }\mu\text{m}$, surface area $2\text{--}5\text{ m}^2\text{ g}^{-1}$) in an ink solution of 3.5 wt.% ethyl cellulose (Fisher Scientific, viscosity 100 cP, 5% in toluene/ethanol 80:20 v/v, extent of labeling: 48% ethoxyl) in α -terpineol (Fisher Scientific, $> 97\%$). Pt slurry was supplied by ESL ElectroScience Inc. (firing residue $> 99.3\%$). Platinum wires were bought from Surepure Chemetals Inc. with the purity of 99.99%.

2.2 Sensor packaging and lab-test station

As shown in Fig. 1f, a two-compartment configuration is used for sensor packaging and testing. NiO acts as the sensing electrode (SE) and is exposed to flowing sample gas or base gas, while Pt acts as the reference electrode (RE) and is always exposed to flowing air. Sample gases, base gases, and air were transported via alumina tubes (Advalue Technology, LLC, $> 99.0\%$). The base gases and sample gases were adjusted via controlling the flowrate of gases from a cylinder of 2000 ppm CO gas (balanced by N_2), a cylinder of air, and a cylinder of N_2 . All gas cylinders were bought from Matheson Tri-Gas, Inc. with purity $> 99.9\%$. Digital mass controllers (Alicat) controlled mass flow rates. A ceramic bond (Aremco Products Inc. 552-VFG-1222) was used for mounting and sealing the sensor pellet on the top of the alumina tube.

2.3 Gas sensing measurements

The sensor signal is measured via recording the electromotive force (EMF) between the SE and RE. NiO SE connected to the working probe (also the positive probe) of the

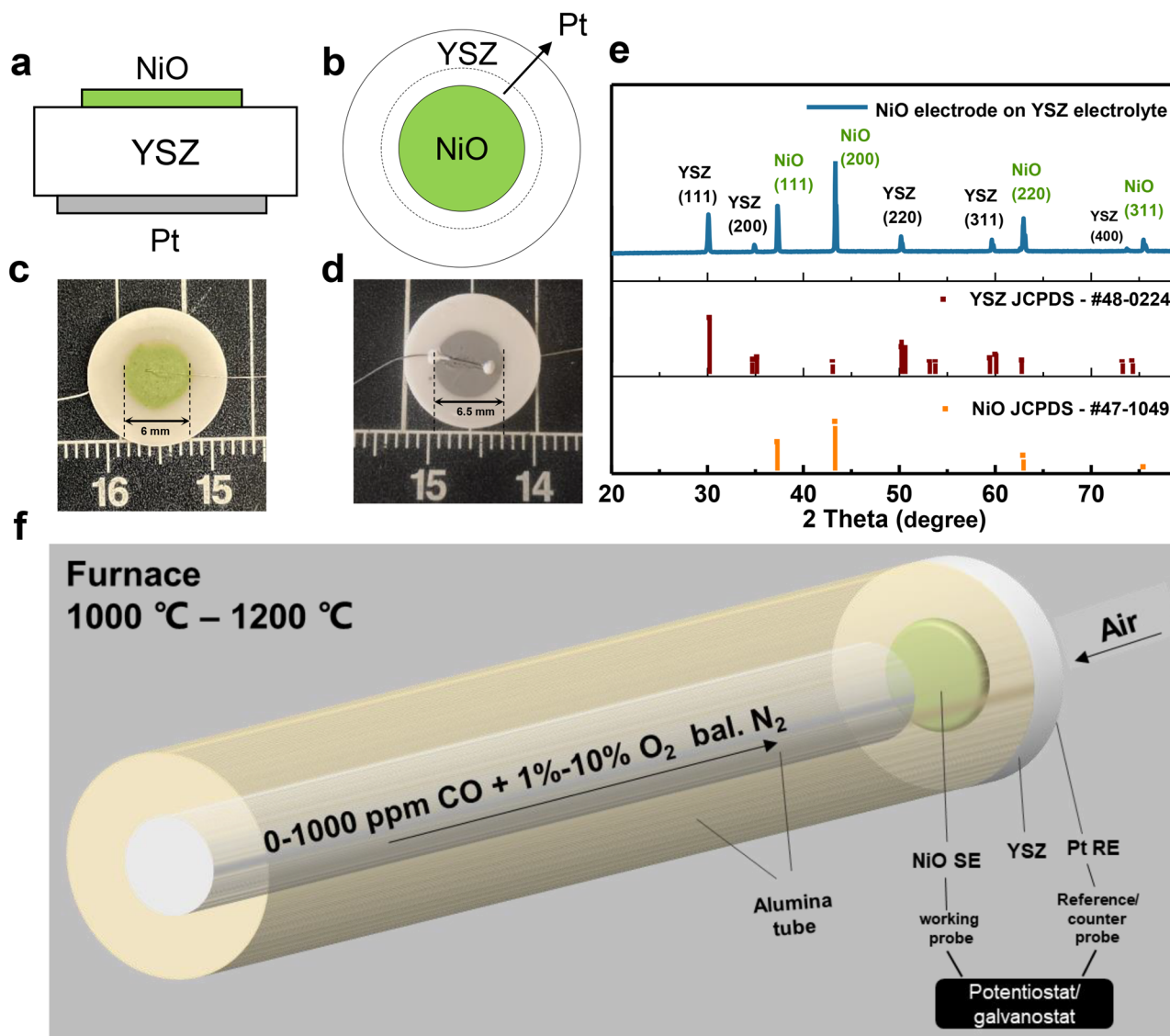


Fig. 1 Schematics of **a** cross-sectional view and **b** top view of the sensor structure. Photographic images of **c** NiO side and **d** Pt side of an as-prepared sensor sample. **e** XRD result of NiO side of the sensor sample and standard XRD cards of NiO and YSZ. **f** Sensor packaging and testing configuration for electrochemical measurements such as

potentiostat and Pt RE connected to the reference probe and counter probe (the negative probe). The potentiostat of Gamry Interface 5000E was used to record the electrochemical data. The sensor signal was measured in the atmosphere of 0–1000 ppm CO and 1–3% O₂ balanced by N₂ with a total 200 sccm (standard cm³ min⁻¹) flowrate at temperature of 1000–1200 °C. This testing arrangement also applies to other electrochemical characterizations in this work such as polarization curve and electrochemical impedance spectroscopy (EIS). EIS was carried out on sensor samples at open circuit condition (without polarization) over 10⁵ to 10⁻¹ Hz frequency range with 10 mV perturbation. The potentiody-

EMF, polarization curve, and EIS. NiO sensing electrode (SE) connects to the working probe and Pt reference electrode (RE) connects to the reference probe and counter probe of the potentiostat/galvanostat equipment

namic polarization curve measurements were carried out from 150 to -150 mV at a scan rate of 1 mV s⁻¹.

2.4 Microscopic, structural, and compositional characterizations

X-ray diffraction (XRD, PANALYTICAL X'Pert Pro) with a 0.02° step size was used to characterize crystal structures of materials. A scanning electron microscope (SEM Hitachi S-4700) was used to characterize the micro-morphologies of each electrode. Thermogravimetric analysis (TGA, SDT650 TA Instruments) was conducted to measure the mass

change of NiO powders under the atmosphere of 1500 ppm CO + 2% O₂, bal. N₂ with a heating rate of 10 °C min⁻¹. X-ray photoelectron spectroscopy (XPS) using a Physical Electronics PHI 5000 Versa Probe spectrometer equipped with a monochromatic Al K α source was applied to analyze the elemental composition and valence states on the surface.

3 Results and discussion

3.1 Sensor structure and lab-test configuration

Figure 1a, b show the schematic cross-sectional view and top view of the sensor structure, respectively. YSZ (2 mm thick) is used as the support and electrolyte. NiO electrode (6 mm diameter) is sintered on the YSZ surface with a thin platinum wire embedded to transmit electrical signals (Fig. 1c). Pt electrode (6.5 mm diameter) is sintered on the counter surface of the YSZ pellet with a Pt wire as the lead wire (Fig. 1d). Figure 1e demonstrates the X-ray diffraction (XRD) result of the NiO side of the as-prepared sensor sample. The XRD pattern of the sintered pellet of NiO electrode on YSZ electrolyte is consistent with the standard XRD cards of NiO (JCPDS #48–0224) and YSZ (JCPDS #47–1049), where clear and clean peaks of NiO and YSZ confirm their crystal structure and show no chemical reactions between them. Figure 1f presents the sensor packaging and testing configuration. A two-compartment configuration is used, where the NiO sensing electrode (SE) is exposed to flowing sample and base gases, while Pt, the reference electrode (RE), is always exposed to flowing air. The sensor signal is measured via recording the electromotive force (EMF) between the SE and RE, with the NiO SE connected to the working probe of the potentiostat and the Pt RE connected to the reference probe and counter probe. Therefore, the measured sensor signal is obtained as follows:

$$EMF = U_{SE} - U_{RE} \quad (1)$$

where U_{SE} is the potential of SE, and U_{RE} is the potential of RE. The sensor response can be calculated as follows:

Table 1 Baseline values of NiO electrode to varied oxygen content under 1000, 1100, and 1200 °C

Oxygen content	Baseline @1000 °C / mV	Baseline @1100 °C / mV	Baseline @1200 °C / mV
1% O ₂ , bal. N ₂	-67.8	-72.6	-79.2
3% O ₂ , bal. N ₂	-43.7	-46.7	-51.5
5% O ₂ , bal. N ₂	-32.5	-34.6	-38.6
10% O ₂ , bal. N ₂	-17.3	-18.3	-21.0

$$Sensor\ Response = EMF_s - EMF_b \quad (2)$$

where EMF_s is the EMF in the sample gas, and EMF_b is the EMF in the base gas (also known as the baseline). This testing arrangement also applies to other electrochemical characterizations in this work such as polarization curve and electrochemical impedance spectroscopy (EIS).

3.2 CO Sensing behavior of NiO at 1000–1200 °C

3.2.1 Influence of feed gas flow rate, NiO electrode thickness, and porosity

Mixed potential is generated from the kinetic balance between chemical and electrochemical reactions occurring over the sensing electrode and electrode/electrolyte interface [50]. Factors that affect the kinetics, such as feed gas flow rate, SE thickness, and porosity, are systematically investigated. Flow rate varies from 100 standard cubic centimeters per minute (sccm) to 300 sccm. Thickness is varied by 21 μ m, 45 μ m, and 60 μ m, designated as T1, T2, and T3. SE porosity is adjusted by adding different content of pore former (PF) by weight ratio in the NiO slurries: 10% PF, 20% PF, and 30% PF. The SEM images of cross sections of NiO/YSZ interfaces are shown in Fig. S1, demonstrating the presence of macropores in the NiO layer. Baseline values are hardly altered by gas transport-related variables, as demonstrated in Figs. S3 and S4. They are linearly fitted and presented in Table 1.

Figure 2a–c demonstrate the sensing behavior to CO of NiO electrodes affected by the three gas transport-related factors: feed gas flow rate, SE thickness, and SE porosity, with baseline values presented via dash lines. In general, a better transport facilitates the sensor sensitivity, as shown in Fig. 2d, e where a higher flow rate and thinner electrode lead to higher responses. This is reasonable since a lower CO amount would be consumed by chemical reactions due to faster gas transport and more CO would reach the tripe-phase boundary (TPB) to form the mixed potential. However, Fig. 2f shows that the 20% PF sensor sample exhibits a higher response than the 30% PF sample does. This might be because the NiO electrode of the 30% PF sample has elevated activity due to the smaller particle size, since pore former inhibits particle growth during the sintering process. The 30% PF sample might consume more CO than the 20% PF sample by chemical reactions that do not generate electrical signals. In addition, in the higher CO content region, responses are linear to the logarithm of CO concentration, indicating that electrochemical reaction is probably the rate-limiting step for CO sensing of NiO at 1000 °C. Figure 2g–i display that response t_{90} (time to achieve 90% final signal magnitude) is generally

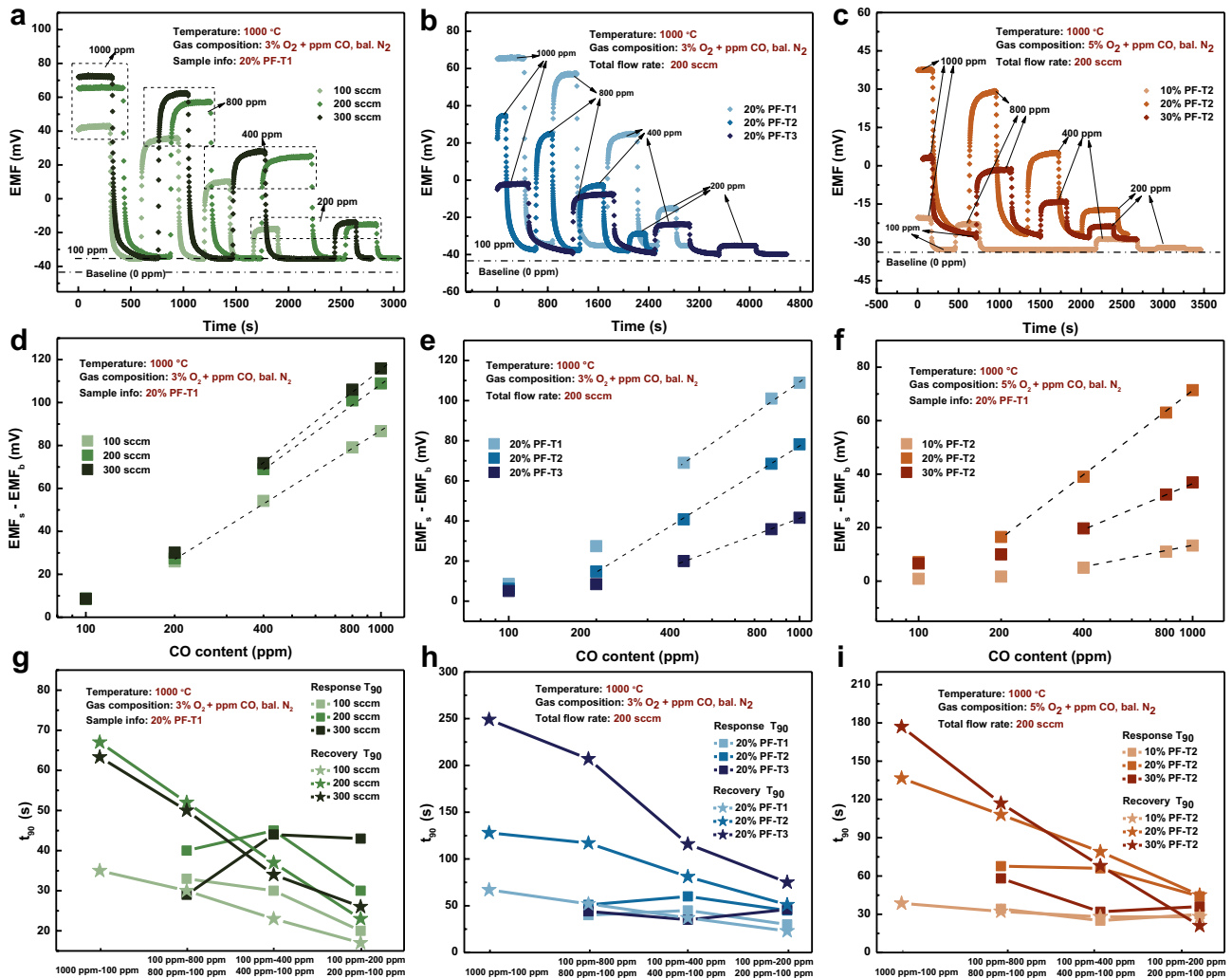


Fig. 2 Sensing behavior (EMF_s vs. time) to CO with varied **a** feed gas flow rate, **b** NiO electrode thickness, and **c** NiO electrode porosity. Dependence of sensor responses ($EMF_s - EMF_b$) on the logarithm of CO content with varied **d** feed gas flow rate, **e** NiO electrode thick-

ness, and **f** NiO electrode porosity. Time to achieve 90% final signal magnitude (t_{90}) of response and recovery with varied **g** feed gas flow rate, **h** NiO electrode thickness, and **i** NiO electrode porosity

smaller than recovery T_{90} , suggesting that CO adsorption is faster than CO desorption.

3.2.2 Influence of oxygen content and temperature on behavior and stability

Figure 3a demonstrates at 1100 °C the influence of oxygen content on the CO sensing property of NiO electrode, with detailed chrono EMF results displayed in Fig. S5a–d. Since responses are clearly neither linear to the logarithm of oxygen concentration (Fig. 3a) nor linear to oxygen concentration (Fig. S5f), weak chemical adsorption of oxygen over NiO surface is possibly the rate-limiting step of the oxygen-NiO reaction, rather than electrochemical reaction or gas diffusion. This is reasonable because at such a high temperature, the sticking probability of oxygen would be

notably decreased [51]. Figure 3b shows that NiO's CO sensitivity is clearly weakened by temperature increase. The sensor response to 1000 ppm CO decreases from 109 mV @ 1000 °C to 7 mV @ 1200 °C. This is possibly because elevated temperatures significantly increase the CO consumption within the NiO electrode before CO reaches the TPB. Figure 3c exhibits a 180 h stability measurement, showing that despite a small drop on the first day, the response is restored after 24 h and remains stable after 48 h. Figure 3d displays the comparison of the initial and final sensing behavior, verifying the robustness of the NiO electrode. Figure 3e and Table S1 present a comparison of sensing performances in this work and reported literature [26, 40, 41, 43, 44, 46, 48, 49]. This work for the first time achieves a notable sensing performance for a mixed potential sensor working at temperatures above 1000 °C to 1000 ppm in

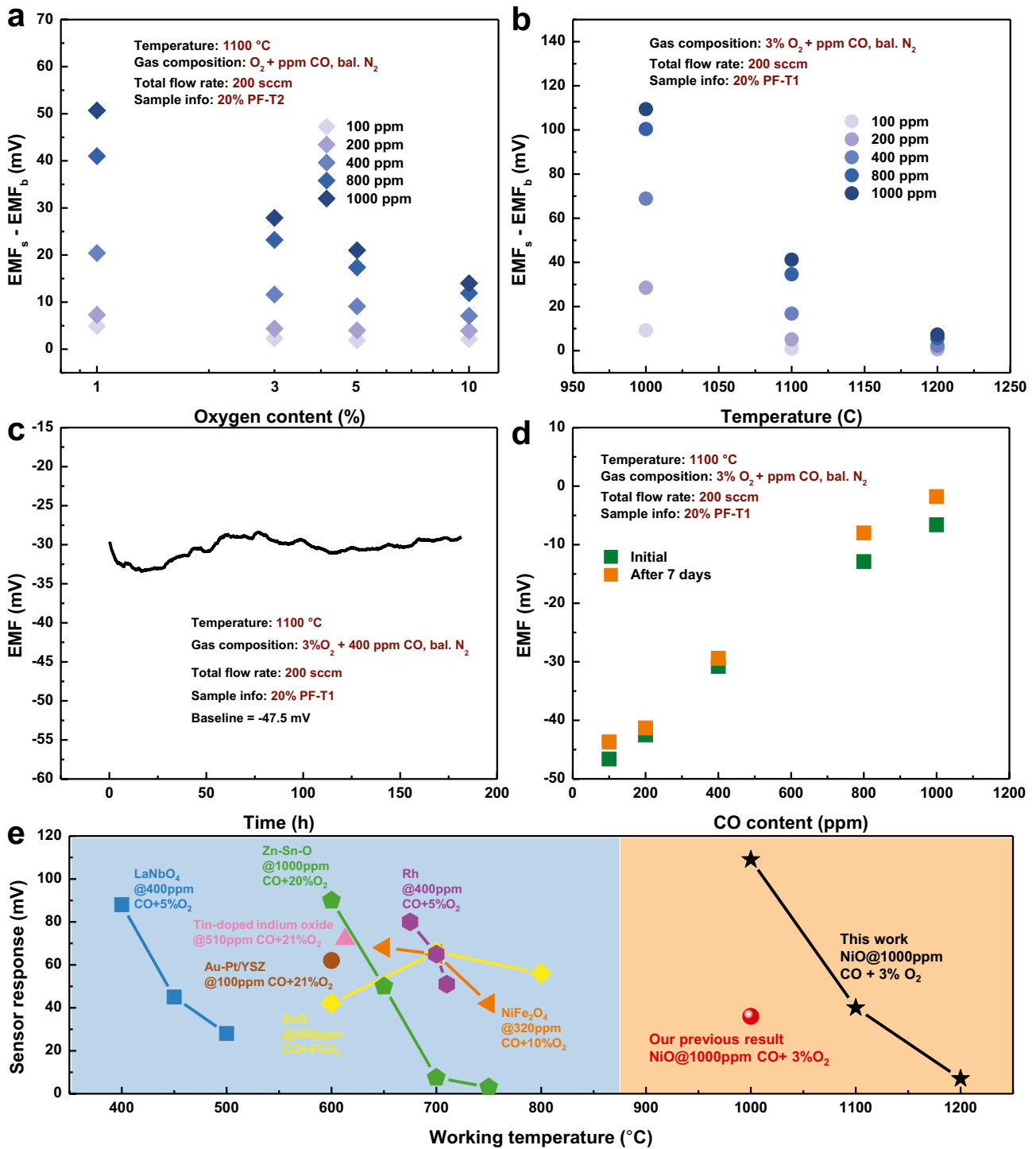


Fig. 3 **a** Sensing responses of NiO electrode at 1100 °C with varied oxygen contents. **b** Sensing responses of NiO electrode at 1000–1200 °C. **c** A stability test for the NiO sensing electrode at 1100 °C to 400 ppm CO + 3% O₂. **d** Sensing performances comparison between the as-prepared sample and that after a 180-h durability test. **e** Summary of sensing performances in this work and recently reported

literature. Data of LaNbO₄ adapted from [10b], data of tin-doped indium oxide adapted from [10j], data of Au-Pt/YSZ adapted from [10f], data of Zn-Sn-O adapted from [10h], data of ZnO adapted from [10c], data of Rh adapted from [10k], data of NiFe₂O₄ adapted from [10e], and data of NiO adapted from [6]

3% O₂: 109 mV @1000 °C, 40 mV @1100 °C, and 7 mV @1200 °C. After comparing the temperature effect on sensing responses and T₉₀, the optimal working temperature for this proposed NiO electrode is 1100 °C due to the acceptable sensitivity and fast response and recovery (<25 s, as seen in Fig. S7).

3.3 CO sensing mechanism of NiO at 1000–1200 °C

For most mixed potential CO sensors reported in the literature, the generated mixed potential of the electrode is negatively related to CO content during the CO sensing process [39–44]. This is because, as shown in the left color block

in Fig. 4a, the potential of CO electrochemical oxidation is more negative than the potential of oxygen reaction (baseline potential). This leads to a negative shift of the formed mixed potential relative to the baseline when the two reactions are equally coupled. Thus, a higher CO content causes a more negative potential and higher response, as demonstrated in Fig. 4a showing $E_{\text{mix}2} < E_{\text{mix}1}$.

However, in our previously reported work [26] and this work, the mixed potential of NiO is surprisingly higher than the baseline and further positively related to CO content in sample gas at 1000–1200 °C. This inverse phenomenon induces the idea that it is a CO-related reduction reaction, instead of CO oxidation, that couples with the oxygen

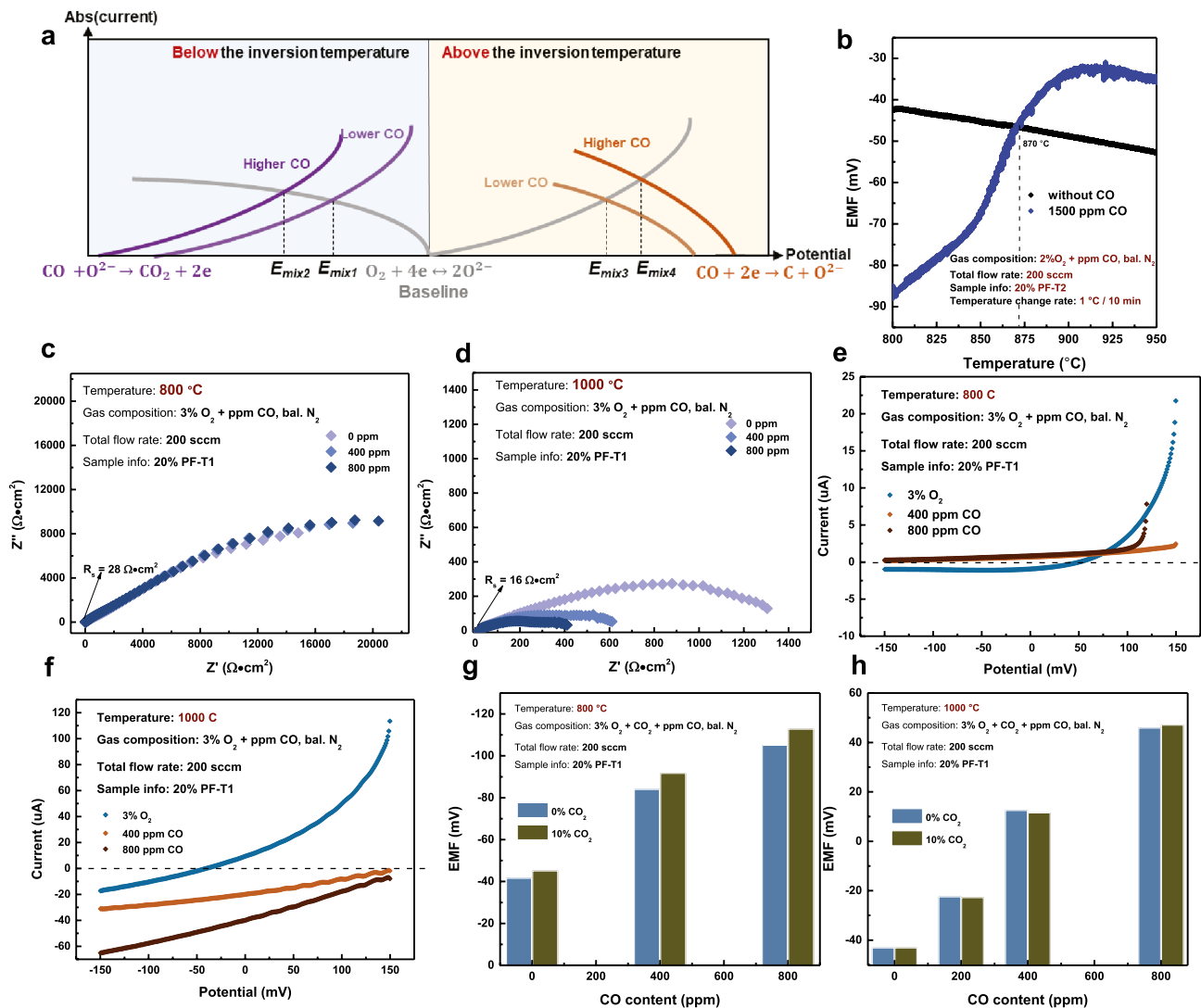


Fig. 4 a Proposed mechanism for the inversion phenomenon and positive relationship between sensor response and CO content. b Steady EMF vs. temperature of NiO at CO containing and non-containing conditions; the temperature scan rate is 1 °C/10 min to ensure steady state. EIS results of NiO electrode to feed gas containing 0 ppm,

400 ppm, and 800 ppm CO at c 800 °C and d 1000 °C. Polarization curve of NiO electrode to 3% O₂ base gas, and modified polarization curve to 400 ppm CO and 800 ppm CO at e 800 °C and f 1000 °C. Sensing behavior of NiO to CO₂ containing atmosphere compared to non-containing CO atmosphere at g 800 °C and h 1000 °C

evolution reaction to form the mixed potential, as shown in the right block in Fig. 4a. Detailed evidence and reasoning for this mechanism is presented as follows.

3.3.1 Electrochemical methods

Figure 4b shows the dependence of the steady EMF values of NiO on temperatures with and without CO in the feed gas. A 1 °C/10 min temperature increase rate is applied to ensure a steady state. It is surprising that the EMF curve of NiO in CO-containing atmosphere intersects the EMF curve in zero CO condition (namely sensing baseline curve) at 870 °C. This phenomenon is particular to the NiO sensor and is not found on Pt electrode. As seen in Fig. S8, the potential of the Pt electrode in the CO-containing sample gas is very closely parallel to the baseline after 600 °C with no intersection observed. To our best knowledge, it is for the first time that an inversion temperature (the intersection 870 °C) is observed for CO sensing. This important inversion temperature discovery could expand the current CO sensing theory by integrating CO oxidation and CO reduction.

To further explore what the specific CO reaction is over NiO above the inversion temperature, the open circuit potential EIS of the NiO electrode is performed in a feed gas of 3%O₂ and varied contents of CO at 800 °C and 1000 °C, as shown in Fig. 4c, d. At 800 °C, the addition of CO slightly increases the reaction resistance, as presented in Fig. 4c. This could be ascribed to the decreased coverage of adsorbed oxygen over NiO since the reaction of oxygen redox pair is the main contributor to the EIS signal and a small amount of adsorbed oxygen is consumed by CO oxidation. However, an evident contrast is that at 1000 °C, the addition of CO significantly reduces the polarization resistance, suggesting that a markable amount of adsorbed oxygen species is generated, as observed in Fig. 4d. This is further supported by the minor effect of pure oxygen content on the polarization resistance as shown in Fig. S9. Figure S9 displays the open circuit potential EIS for NiO electrode in base gas with varied oxygen contents at 1000 °C. The oxygen content increase only marginally reduces the reaction resistance. This suggests that oxygen molecule dissociation and adsorption over NiO surface at high temperatures is weak, in agreement with the result of Fig. 3a. Therefore, the following half-reaction (Eq. 3) is proposed concerning CO reduction, coupling the oxygen evolution reaction (Eq. 4) to form a positively shifted mixed potential regarding the baseline, as explicitly demonstrated in Fig. 4a.



A modified polarization curve is obtained by subtracting the polarization curve of SE in baseline gas from that in the sample gas. It exclusively elucidates the polarized behavior of SE due to CO. In agreement with the proposed mechanism in Fig. 4a, the modified polarization curves of 400 ppm and 800 ppm CO at 800 °C exhibit anodic currents (Fig. 4e) indicating CO oxidation, while at 1000 °C, they display cathodic currents (Fig. 4f) indicating CO reduction.

The results of CO₂ effects on sensing behavior of NiO under different temperatures can further justify the proposed mechanism, as shown in Fig. 4g, h. At 800 °C, the existence of CO₂ clearly lowers the measured EMF values, indicating an enhanced sensing response of the NiO electrode to CO. This might be because the adsorption of CO₂ is competing with O₂ adsorption, leading to a lowered oxygen coverage and thus a compromised oxygen reduction activity and a promoted CO sensitivity [39]. In contrast, at 1000 °C, there is essentially no difference between the sensing signal to CO of NiO for conditions with or without CO₂ (Fig. 4h), which is in agreement with the proposed mechanism that CO₂ is not participating the CO reduction reaction. The detailed chrono-EMF measurement results of NiO with and without CO₂ at 1000 °C is demonstrated in Fig. S10.

3.3.2 Microscopic, structural, and compositional characterizations

Since the proposed mechanism also claims the generation of C over NiO in addition to oxygen ions (Eq. 3), this mechanism would be strongly supported if carbon is detected. Therefore, to amplify the outcome of CO-NiO interaction above the inversion temperature, a 3-day atmospheric treatment at 1000 °C was applied to two NiO sensor samples, with one annealed in base gas (2% O₂, bal. N₂) and the other one annealed in the corresponding sample gas containing 1000 ppm CO. Constant gas compositions are maintained by flowing the gases.

Figure 5a shows the color change of treated NiO electrodes when CO exists in the atmosphere. NiO becomes darker when the treatment gas contains 1000 ppm CO, while the color of NiO treated in the base gas is nearly identical with the as-prepared sample as shown in Fig. 1c. According to literature [52], excessive oxygen in the NiO structure would cause the color of NiO to become darker. Although Fig. 5a does not suggest the production of carbon, it supports the mechanism since more oxygen is possibly generated.

XRD and thermal gravimetric analysis (TGA) measurements do not detect any obvious difference for the two treated NiO electrodes, as shown in Figs. 5b and S11. However, SEM images of the two treated NiO electrodes demonstrate significant nanoscale morphological differences. Compared to base gas treatment, the particles of CO-treated NiO are more sharpened, with a large number of defects and

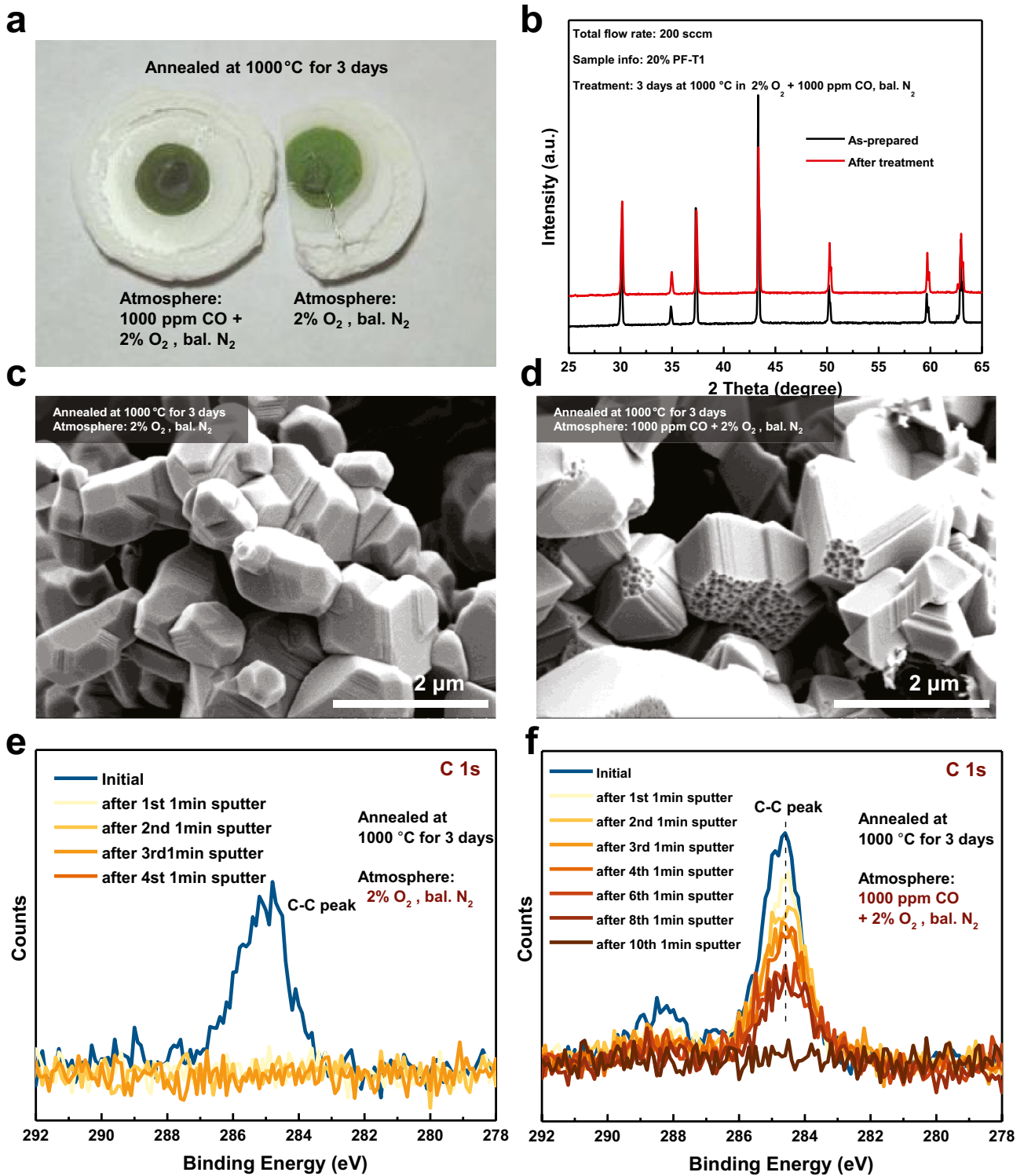


Fig. 5 **a** Photographic images of sensor samples after 3-day atmospheric treatments at 1000 °C with CO and without CO. **b** XRD results of NiO electrodes before and after 3-day atmospheric treatments at 1000 °C with CO. SEM images of NiO electrodes after the

3-day atmospheric treatments at 1000 °C **c** without CO and **d** with CO. XPS results of carbon peak of NiO electrodes after the 3-day atmospheric treatments at 1000 °C **e** without CO and **f** with CO

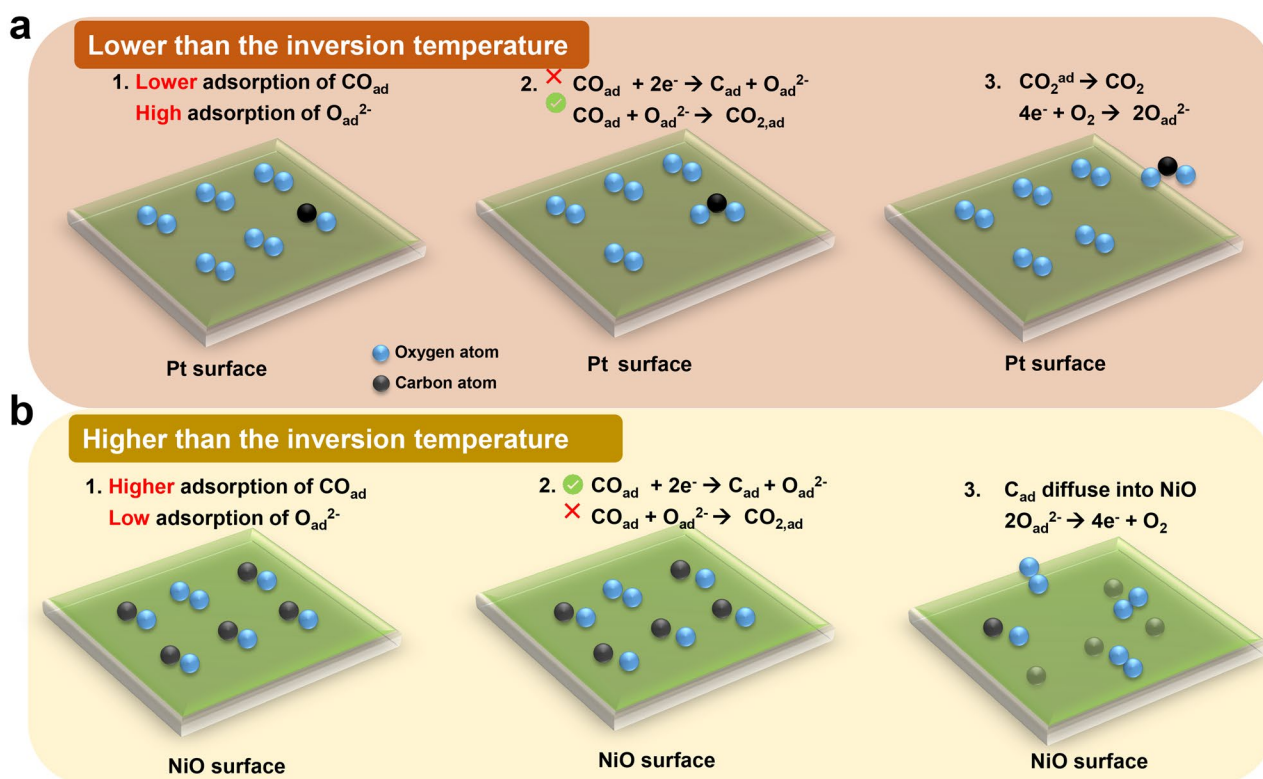


Fig. 6 Proposed mechanisms of CO sensing over NiO surfaces **a** below and **b** above the inversion temperature

clear stairs observed on some specific facets. Combined with the XRD and TGA results, the CO-NiO interactions above the inversion temperatures are believed to focus on the surface region. Therefore, depth-resolved X-ray photoelectron spectroscopy (XPS) measurements were performed on the two treated sensor samples, as shown in Figs. 5e, f and S12. For the baseline gas-treated NiO, the carbon peak is diminished after the first 1-min Ar^+ sputtering (corresponding to ~ 2 nm Fig. 5e). In contrast, carbon has not disappeared until the 10th sputtering for the NiO treated in a CO-containing atmosphere (Fig. 5f). While the initial carbon signal can be attributed to the contamination of residue carbons, the clear carbon peaks after each sputter process, although small, prove the generation of carbon and further justify the proposed mechanism. The result also suggests that the produced C by CO reduction dissolves into NiO phase. Figure S12 shows the XPS results of oxygen and nickel of CO-treated NiO. Although Ni_2O_3 peaks are observed, the results are not believed as strong evidence since the valence of Ni can be altered by Ar^+ sputtering [53–56], which also affects oxygen's coordination. The XPS results of carbon are very convincing as carbon is barely affected by Ni^{2+} reduction during sputtering.

Thus, since the CO decomposition is of particularity (occurs over NiO not over Pt), it is preferential to examine

the thermodynamics of adsorbed species, such as CO_{ad} , $\text{O}_{\text{ad}}^{2-}$, $\text{CO}_{2,\text{ad}}$, and C_{ad} . Therefore, we propose the mechanism as shown in Fig. 6. When temperature is lower than the inversion temperature, the coverage of oxygen adsorbed species ($\text{O}_{\text{ad}}^{2-}$) on NiO would be much higher than the adsorbed CO (CO_{ad}), as shown in Fig. 6a step 1. This leads to a higher driving force of CO oxidation forming CO_2 (steps 2 and 3 in Fig. 6a). In contrast, when temperature is above the inversion temperature, the adsorption of oxygen over NiO is weak, while the adsorption of CO is more energetically favorable. Thus, the coverage of CO (CO_{ad}) is much higher than $\text{O}_{\text{ad}}^{2-}$ (step 1, Fig. 6b), resulting in favorable energy for CO decomposition (step 2, Fig. 6b). Therefore, CO is decomposed over these surfaces with a portion of carbon diffusing into the NiO (step 3, Fig. 6b).

4 Conclusions

This work presents a well-functioning mixed potential CO gas sensor using NiO as the sensing electrode at 1000–1200 °C, demonstrating its potential to be used as an in situ gas sensor in a utility boiler. A larger flow rate and thinner thickness facilitate the sensitivity, suggesting that better gas transport promotes an improved sensitivity.

However, the 20% PF sample exhibits better responses than the 30% PF sample, indicating the importance of the chemical/electrochemical reaction balance. Notable and fast responses to 1000 ppm in 3% O₂ are reported: 109 mV @ 1000 °C, 40 mV @ 1100 °C, and 7 mV @ 1200 °C. Differences of EIS results of NiO at 800 °C and 1000 °C in CO-containing atmosphere demonstrate that CO releases oxygen ions over NiO surface considerably at 1000 °C because the resistance reaction is significantly reduced when CO exists. The depth-resolved XPS results of carbon in NiO electrodes treated at 800 °C and 1000 °C prove that the carbon is produced via CO-NiO reaction and dissolves into NiO lattice. These observations justify a mechanism that CO is electrochemically reduced over NiO into carbon and oxygen ions. The CO reduction reaction coupled with the oxygen evolution reaction leads to the positive relationship between the NiO electrode's mixed potential and CO content. Furthermore, an inversion temperature is found for the CO-NiO reaction for the first time, showing the union of the commonly reported CO oxidation-based and the proposed CO reduction-based mechanism.

Supplementary information The online version contains supplementary material available at <https://doi.org/10.1007/s42114-022-00480-9>.

Acknowledgements We would like to thank the program managers John Rockey, Sydni Credle, and Barbara Carney for the technical guidance and financial support. We also acknowledged the use of the WVU Shared Research Facilities and managers Dr. Qiang Wang and Dr. Marcela Redigolo.

Funding The US Department of Energy, National Energy Technology Laboratory (NETL) financially supported this work under the contract number DE-FE31564.

Declarations

Conflict of interest The authors declare no competing interests.

References

- Aguilera RF, Aguilera R (2020) Revisiting the role of natural gas as a transition fuel. *Miner Econ* 33(1):73–80. <https://doi.org/10.1007/s13563-019-00192-5>
- Waqas M, Kouotou PM, Kasmi AE, Wang Y, Tian Z-Y (2018) Facile synthesis of efficient Cu-Co-Fe ternary oxides by pulsed-spray evaporation CVD for CO oxidation. *ES Energy Environ* 1:67–73. <https://doi.org/10.30919/esee8c145>
- Dey S, Dhal GC, Mohan D, Prasad R (2020) Structural and catalytic properties of Fe and Ni doping on CuMnO_x catalyst for CO oxidation. *Adv Compos Hybrid Mater* 3(1):84–97. <https://doi.org/10.1007/s42114-020-00139-3>
- E J, Ding J, Chen J, Liao G, Zhang F, Luo B (2021) Process in micro-combustion and energy conversion of micro power system: a review. *Energy Convers Manag* 246:114664. <https://doi.org/10.1016/j.enconman.2021.114664>
- Nejat P, Jomehzadeh F, Taheri MM, Gohari M, Majid MZA (2015) A global review of energy consumption, CO₂ emissions and policy in the residential sector (with an overview of the top ten CO₂ emitting countries). *Renew Sustain Energy Rev* 43:843–862. <https://doi.org/10.1016/j.rser.2014.11.066>
- Sun J, Mu Q, Kimura H, Murugadoss V, He M, Du W, Hou C (2022) Oxidative degradation of phenols and substituted phenols in the water and atmosphere: a review. *Adv Compos Hybrid Mater*. <https://doi.org/10.1007/s42114-022-00435-0>
- Ma Y, Xie X, Yang W, Yu Z, Sun X, Zhang Y, Yang X, Kimura H, Hou C, Guo Z, Du W (2021) Recent advances in transition metal oxides with different dimensions as electrodes for high-performance supercapacitors. *Adv Compos Hybrid Mater* 4(4):906–924. <https://doi.org/10.1007/s42114-021-00358-2>
- Hou C, Wang B, Murugadoss V, Vupputuri S, Chao Y, Guo Z, Wang C, Du W (2020) Recent advances in Co₃O₄ as anode materials for high-performance lithium-ion batteries. *Eng Sci* 11:19–30. <https://doi.org/10.30919/es8d1128>
- Cheng XQ, Li S, Bao H, Yang X, Li Z, Zhang Y, Wang K, Ma J, Ullah A, Shao L (2021) Poly(sodium-p-styrenesulfonate)-grafted UiO-66 composite membranes boosting highly efficient molecular separation for environmental remediation. *Adv Compos Hybrid Mater* 4(3):562–573. <https://doi.org/10.1007/s42114-021-00253-w>
- Lin C, Liu B, Pu L, Sun Y, Xue Y, Chang M, Li X, Lu X, Chen R, Zhang J (2021) Photocatalytic oxidation removal of fluoride ion in wastewater by g-C₃N₄/TiO₂ under simulated visible light. *Adv Compos Hybrid Mater* 4(2):339–349. <https://doi.org/10.1007/s42114-021-00228-x>
- Sutton J, Spinney P (2016) Digital, interconnected power plants to improve efficiency and reduce emissions. <https://www.nicenergy.com/dtywyyw/djs/201911/f8afb64e5f4e4ce0a91979a0866c0b0e/files/7f7210e24fed4b72b14d418ae4c2dd96.pdf>
- Huang Y, Luo Y, Liu H, Lu X, Zhao J, Lei Y (2021) A subcutaneously injected SERS nanosensor enabled long-term in vivo glucose tracking. *Eng Sci* 14:59–68. <https://doi.org/10.30919/es8d1161>
- Gijare M, Chaudhari S, Ekar S, Garje A (2021) Reduced graphene oxide based electrochemical nonenzymatic human serum glucose sensor. *ES Mater Manuf* 14:110–119. <https://doi.org/10.30919/esmm5f486>
- Su Y-F, Han G, Kong Z, Nantung T, Lu N (2020) Embeddable piezoelectric sensors for strength gain monitoring of cementitious materials: the influence of coating materials. *Eng Sci* 11:66–75. <https://doi.org/10.30919/es8d1114>
- Chang X, Chen L, Chen J, Zhu Y, Guo Z (2021) Advances in transparent and stretchable strain sensors. *Adv Compos Hybrid Mater* 4(3):435–450. <https://doi.org/10.1007/s42114-021-00292-3>
- Jiang N, Hu D, Xu Y, Chen J, Chang X, Zhu Y, Li Y, Guo Z (2021) Ionic liquid enabled flexible transparent polydimethylsiloxane sensors for both strain and temperature sensing. *Adv Compos Hybrid Mater* 4(3):574–583. <https://doi.org/10.1007/s42114-021-00262-9>
- Li G-Y, Li J, Li Z-J, Zhang Y-P, Zhang X, Wang Z-J, Han W-P, Sun B, Long Y-Z, Zhang H-D (2021) Hierarchical PVDF-HFP/ZnO composite nanofiber-based highly sensitive piezoelectric sensor for wireless workout monitoring. *Adv Compos Hybrid Mater*. <https://doi.org/10.1007/s42114-021-00331-z>
- Hu M, Gao Y, Jiang Y, Zeng H, Zeng S, Zhu M, Xu G, Sun L (2021) High-performance strain sensors based on bilayer carbon black/PDMS hybrids. *Adv Compos Hybrid Mater* 4(3):514–520. <https://doi.org/10.1007/s42114-021-00226-z>
- Zhai Y, Yang W, Xie X, Sun X, Wang J, Yang X, Naik N, Kimura H, Du W, Guo Z, Hou C (2022) Co₃O₄ nanoparticle-dotted hierarchical-assembled carbon nanosheet framework catalysts with the formation/decomposition mechanisms of Li₂O₂ for smart lithium–oxygen batteries. *Inorg Chem Front* 9(6):1115–1124. <https://doi.org/10.1039/D1QI01260F>

20. Hou C, Yang W, Xie X, Sun X, Wang J, Naik N, Pan D, Mai X, Guo Z, Dang F, Du W (2021) Agaric-like anodes of porous carbon decorated with MoO₂ nanoparticles for stable ultralong cycling lifespan and high-rate lithium/sodium storage. *J Colloid Interface Sci* 596:396–407. <https://doi.org/10.1016/j.jcis.2021.03.149>
21. Guo J, Li X, Liu H, Young DP, Song G, Song K, Zhu J, Kong J, Guo Z (2021) Tunable magnetoresistance of core-shell structured polyaniline nanocomposites with 0-, 1-, and 2-dimensional nanocarbons. *Adv Compos Hybrid Mater* 4(1):51–64. <https://doi.org/10.1007/s42114-021-00211-6>
22. Guo J, Chen Z, Abdul W, Kong J, Khan MA, Young DP, Zhu J, Guo Z (2021) Tunable positive magnetoresistance of magnetic polyaniline nanocomposites. *Adv Compos Hybrid Mater* 4(3):534–542. <https://doi.org/10.1007/s42114-021-00242-z>
23. Guo J, Chen Z, Xu X, Li X, Liu H, Xi S, Abdul W, Wu Q, Zhang P, Xu BB, Zhu J, Guo Z (2022) Enhanced electromagnetic wave absorption of engineered epoxy nanocomposites with the assistance of polyaniline fillers. *Adv Compos Hybrid Mater*. <https://doi.org/10.1007/s42114-022-00417-2>
24. Guo J, Li X, Chen Z, Zhu J, Mai X, Wei R, Sun K, Liu H, Chen Y, Naik N, Guo Z (2022) Magnetic NiFe₂O₄/Polypyrrole nanocomposites with enhanced electromagnetic wave absorption. *J Mater Sci Technol* 108:64–72. <https://doi.org/10.1016/j.jmst.2021.08.049>
25. Shuk P, McGuire C (2017) Carbon monoxide gas sensing technologies in combustion process. *Sens Transducers* 217(11):1–13
26. Wang Y, Ma L, Li WY, Li W, Liu X (2020) A high-temperature mixed potential CO gas sensor for in situ combustion control. *J Mater Chem A* 8(38):20101–20110. <https://doi.org/10.1039/D0TA06320G>
27. Liu F, Duncan BN, Krotkov NA, Lamsal LN, Beirle S, Griffin D, McLinden CA, Goldberg DL, Lu Z (2020) A methodology to constrain carbon dioxide emissions from coal-fired power plants using satellite observations of co-emitted nitrogen dioxide. *Atmos Chem Phys* 20(1):99–116. <https://doi.org/10.5194/acp-20-99-2020>
28. Kamas J, Keeler J (1995) Predictive emissions monitoring systems: a low-cost alternative for emissions monitoring [in cement industry]. In: 1995 IEEE Cement Industry Technical Conference. 37th Conference Record, pp 497–509. <https://doi.org/10.1109/CITCON.1995.514350>
29. Rohilla D, Chaudhary S, Umar A (2021) An overview of advanced nanomaterials for sensor applications. *Eng Sci* 16:47–70. <https://doi.org/10.30919/es8d552>
30. Wang D, Yin Y, Xu P, Wang F, Wang P, Xu J, Wang X, Li X (2020) The catalytic-induced sensing effect of triangular CeO₂ nanoflakes for enhanced BTEX vapor detection with conventional ZnO gas sensors. *J Mater Chem A* 8(22):11188–11194. <https://doi.org/10.1039/D0TA01708F>
31. Purbia R, Kwon YM, Kim H-D, Lee YS, Shin H, Baik JM (2020) Zero-dimensional heterostructures: N-doped graphene dots/SnO₂ for ultrasensitive and selective NO₂ gas sensing at low temperatures. *J Mater Chem A* 8(23):11734–11742. <https://doi.org/10.1039/D0TA03037F>
32. Lu Y, Li W, Zhang J, Liu Y, Casey P, Bateman S, Shen SZ, Zhou J, Zakharova GS, Chen W (2015) Preparation and room temperature gas sensing study of tungsten oxide nanowires/PEDOT/PSS hybrid materials. *Ferroelectrics* 477(1):93–102. <https://doi.org/10.1080/00150193.2015.1000114>
33. Prabhu NN, Chandra RBJ, Rajendra BV, George G, Mourad A-HI, Shivamurthy B (2022) Electrospun ZnO nanofiber based resistive gas/vapor sensors -a review. *Eng Sci* 19:59–82. <https://doi.org/10.30919/es8d612>
34. Chen J, Zhu Y, Guo Z, Nasibulin AG (2020) Recent progress on thermo-electrical properties of conductive polymer composites and their application in temperature sensors. *Eng Sci* 12:13–22. <https://doi.org/10.30919/es8d1129>
35. Umar A, Kumar R, Algadi H, Ahmed J, Jalalah M, Ibrahim AA, Harraz FA, Alsaiari MA, Albargi H (2021) Highly sensitive and selective 2-nitroaniline chemical sensor based on Ce-doped SnO₂ nanosheets/Nafion-modified glassy carbon electrode. *Adv Compos Hybrid Mater* 4(4):1015–1026. <https://doi.org/10.1007/s42114-021-00283-4>
36. Li W, Zhang L-S, Wang Q, Yu Y, Chen Z, Cao C-Y, Song W-G (2012) Low-cost synthesis of graphitic carbon nanofibers as excellent room temperature sensors for explosive gases. *J Mater Chem* 22(30):15342–15347. <https://doi.org/10.1039/C2JM32031B>
37. Mishra S, Chaudhary P, Yadav BC, Umar A, Lohia P, Dwivedi DK (2021) Fabrication and characterization of an ultrasensitive humidity sensor based on chalcogenide glassy alloy thin films. *Eng Sci* 15:138–147. <https://doi.org/10.30919/es8d500>
38. Shuk P, McGuire C, Brosha E (2019) Methane gas sensing technologies in combustion: Comprehensive review. *Sens Transducers* 229(1):1–10
39. Zhang X, Kohler H, Schwotzer M, Wu YH, Guth U (2019) Layered Au, Pt-YSZ mixed potential gas sensing electrode: Correlation among sensing response, dynamic electrochemical behavior and structural properties. *Sens Actuators B Chem* 278:117–125. <https://doi.org/10.1016/j.snb.2018.09.073>
40. Liu H, Yu H, Wang J, Xia F, Wang C, Xiao J (2022) LaNbO₄ as an electrode material for mixed-potential CO gas sensors. *Sens Actuators B Chem* 352:130981. <https://doi.org/10.1016/j.snb.2021.130981>
41. Mahendraprabhu K, Selva Sharma A, Elumalai P (2019) CO sensing performances of YSZ-based sensor attached with sol-gel derived ZnO nanospheres. *Sens Actuators B Chem* 283:842–847. <https://doi.org/10.1016/j.snb.2018.11.164>
42. Nematbakhsh Abkenar G, Rieu M, Breuil P, Viricelle J-P (2021) Development of a selective ammonia YSZ-based sensor and modeling of its response. *Sens Actuators B Chem* 338:129833. <https://doi.org/10.1016/j.snb.2021.129833>
43. Yang B, Wang C, Xiao R, Yu H, Wang J, Xu J, Liu H, Xia F, Xiao J (2019) CO response characteristics of NiFe₂O₄ sensing material at elevated temperature. *J Electrochem Soc* 166:B956–B960. <https://doi.org/10.1149/2.0581912jes>
44. Zhang X, Kohler H, Schwotzer M, Guth U (2021) Stability improvement of layered Au, Pt-YSZ mixed-potential gas sensing electrodes by cathodic polarization: studies by steady state and dynamic electrochemical methods. *Sens Actuators B Chem* 342:130065. <https://doi.org/10.1016/j.snb.2021.130065>
45. Anggraini SA, Fujio Y, Ikeda H, Miura N (2017) YSZ-based sensor using Cr-Fe-based spinel-oxide electrodes for selective detection of CO. *Anal Chim Acta* 982:176–184. <https://doi.org/10.1016/j.aca.2017.06.010>
46. Sun F, Li X, Liu L, Wang J (2013) Novel Zn–M–O (M=Sn, Co) sensing electrodes for selective mixed potential CO/C₃H₈ sensors. *Sens Actuators B Chem* 184:220–227. <https://doi.org/10.1016/j.snb.2013.04.002>
47. Liang XS, Yang SQ, Zhong TG, Diao Q, Zhang H, Li JG, Quan BF, Lu GY (2011) Mixed potential type carbon monoxide sensor utilizing NASICON and spinel type oxide electrode. *Sens Lett* 9(2):832–836. <https://doi.org/10.1166/sl.2011.1625>
48. Li X, Xiong W, Kale GM (2005) Novel nanosized ITO electrode for mixed potential gas sensor. *Electrochem Solid-State Lett* 8(3):H27. <https://doi.org/10.1149/1.1854778>
49. Plashnitsa VV, Anggraini SA, Miura N (2011) CO sensing characteristics of YSZ-based planar sensor using Rh-sensing electrode composed of tetrahedral sub-micron particles. *Electrochem Commun* 13(5):444–446. <https://doi.org/10.1016/j.elecom.2011.02.016>
50. Ritter T, Lattus J, Hagen G, Moos R (2019) A finite element model for mixed potential sensors. *Sens Actuators B Chem* 287:476–485. <https://doi.org/10.1016/j.snb.2019.02.052>

51. Bidrawn F, Küngas R, Vohs JM, Gorte RJ (2011) Modeling impedance response of SOFC cathodes prepared by infiltration. *J Electrochem Soc* 158(5):B514. <https://doi.org/10.1149/1.3565174>
52. Newman R, Chrenko RM (1959) Optical properties of nickel oxide. *Phys Rev* 114(6):1507–1513. <https://doi.org/10.1103/PhysRev.114.1507>
53. Chen YS, Kang JF, Chen B, Gao B, Liu LF, Liu XY, Wang YY, Wu L, Yu HY, Wang JY, Chen Q, Wang EG (2012) Microscopic mechanism for unipolar resistive switching behaviour of nickel oxides. *J Phys D Appl Phys* 45(6):065303. <https://doi.org/10.1088/0022-3727/45/6/065303>
54. Payne BP, Biesinger MC, McIntyre NS (2012) Use of oxygen/nickel ratios in the XPS characterisation of oxide phases on nickel metal and nickel alloy surfaces. *J Electron Spectrosc Relat Phenom* 185(5):159–166. <https://doi.org/10.1016/j.elspec.2012.06.008>
55. Chia-Ching W, Cheng-Fu Y (2013) Investigation of the properties of nanostructured Li-doped NiO films using the modified spray pyrolysis method. *Nanoscale Res Lett* 8(1):33. <https://doi.org/10.1186/1556-276X-8-33>
56. Al-Kuhaili M, Ahmad S, Durrani S, Faiz M, Ul-Hamid A (2015) Application of nickel oxide thin films in NiO/Ag multilayer energy-efficient coatings. *Mater Sci Semicond Process* 39:84–89. <https://doi.org/10.1016/j.mssp.2015.04.049>

Publisher's Note Springer Nature remains neutral with regard to jurisdictional claims in published maps and institutional affiliations.